Use of Simulations in Determination of Wheel Impact Forces P1 and P2 Due to Rail Dip Defects

Yan Quan Sun[1], Colin Cole[1], Malcolm Kerr[2] & Sak Kaewunruen[2]
[1]Centre for Railway Engineering, CQ University, Australia
Email: y.q.sun@cqu.edu.au; Tel: 07 49309287
[2]RailCorp, NSW

Abstract
A rail vehicle-track interaction dynamics model has been applied to determine the track vertical dynamic forces due to rail dip defects such as dip joints and welds, which are required in railway vehicle acceptance procedure. The model was validated using the field measurement data of rail dip defects and accelerations of a vehicle axlebox. The simulated dynamic forces – the P2 forces have been compared with those calculated using a well-known formula. Their difference and the formula's limitation have been discussed. The effects of the rail dip defect and the vehicle speed on the track vertical dynamic force have also been investigated.

1. Introduction

The field testing for the determination of railway track vertical dynamic forces, as one of railway vehicle acceptance procedures, would be expensive, complex and time consuming. Alternatively, the use of some formulas to calculate these forces could cause the errors. The advanced simulation techniques can improve this and can be taken as a substitution of test work or simple calculation. In this case, significant savings of time and money and, more importantly, safety is not compromised.

When rail vehicles run over a track with rail dip defects such as dipped weld joints, the dynamic forces generated on the wheel-rail interface inevitably cause deterioration and damage to the track. As a result, the push for higher axle load and faster trains risks more adverse maintenance and safety outcomes. Safe operation of vehicle and track system requires that the maximum permissible force levels are clearly defined and reasonably determined.

As one of the limits, the maximum permissible P_2 force levels have been stipulated by many railway authorities to restrict access of new vehicles into network, e.g. P_2 < 200kN for a vehicle running through a dip angle with 0.01 radian at its nominal maximum speed and nominal gross mass for interstate network in Australia. Forces P_1 and P_2 were originally used by Jenkins et al [1] to term the peak values of track vertical dynamic forces (or wheel dynamic forces), which occur when a wheel travels across a classical dipped rail joint, or a dipped weld joint. The P_1 force is a very high frequency (>>100 Hz) force, which is superimposed on P_2 force and is due to the inertia of the rail. Its effects are largely limited to rail surface failure. The P_2 force occurs at a lower frequency (30 ~ 90 Hz) than the P_1 force. The P_2 force is principally responsible for causing the unsprung mass and the rail/sleeper mass to move down together, causing concrete sleeper breakage and ballast hardening. For this reason, P_2 is of great interest to the railway operators. The following formula, Eq. (1) is widely used to calculate P_2:

$$P_2 = P_0 + 2\alpha V \left[\frac{M_u}{M_u + M_t}\right]^{0.5} \times \left[1 - \frac{C_t \pi}{4[K_t(M_u + M_t)]^{0.5}}\right] \times [K_t M_u]^{0.5} \quad (1)$$

Where P_0 is the static wheel load (kN), M_u is the vehicle unsprung mass (kg), 2α is the total dip joint angle (rad), V is the speed of vehicle (m/s), K_t is the equivalent track stiffness (MN/m), C_t is the equivalent track damping (kNs/m) and M_t is the equivalent track mass (kg).

The current P_2 force formula is not without limitations and further investigations are required to consider the following:

- The inadequate definition of unsprung mass. P_2 would be least accurately calculated for widely used three-piece bogie wagons due to wedge friction in secondary suspension.
- The non-linear relationship between P_2 and dip joint angle.
- The non-linear relationship between P_2 and travel speed.
- The relationship between P_2, track equivalent stiffness, damping and mass parameters.
- The selection or calculation of track equivalent stiffness, damping and mass, e.g. K_t = 109 MN/m, C_t = 52 kNs/m and M_t = 133 kg as given in a procedure [11].
- The use of the same P_2 limits for freight wagons and the application of P_2 limits to higher speed.
- Ignorance of P_1 limit.

A cost-effective method to accurately determine the wheel dynamic forces (including P_1 and P_2 forces) is through simulation. Several theoretical simulation methods have been developed to determine the wheel

dynamic forces. A wheel/rail and track dynamic interaction model was developed by Cai [2] to calculate the wheel-rail impact forces. A similar model to that by Cai [2] was applied by Dahlberg [3] to investigate the effect of rail pads to the wheel dynamic forces. A vehicle-track model was used by Shen [4] to determine the wheel-rail vertical and lateral dynamic forces and the methods to reduce the dynamic forces were put forward. A finite element model of railway track was generated by Dong et al [5] to determine the wheel dynamic forces. Zarembski [6] provided a plot of the relationship between P_1 and P_2 with the unsprung mass, the track modulus and the track mass. The relationship between the geometry of rail welds and the dynamic wheel–rail response was obtained through numerical simulation by Steenbergen and Esveld [7] to assess the rail weld condition. A three dimensional vehicle–track coupled dynamics model was developed by Zhai et al [8] to investigate the dynamics of overall vehicle–track systems

In this paper, a three-dimensional vehicle-track system dynamics model (Sun et al [9], [10]), simply called CRE-3DVTSD model, has been applied. The three translational and three rotational movements of all rail vehicle components – vehicle car body, two bolsters, two sideframes and four wheelsets were considered. The track model employed a discretely supported distributed parameter system with one layer. The simulation results have been validated using the data of manually measured rail dip defects and the data of a vehicle axlebox acceleration measurement.

Forces P_1 and P_2 have been determined through simulation. The comparison between the simulation results and the results using Eq. (1) are also presented and discussed. The railway vehicle acceptance procedures may then be structured around the simulated P_2 force limits.

2. Railway Vehicle-Track Interaction Dynamics Modelling

In this section, the vehicle-track modelling is illustrated and described. Our previous work on vehicle-track interaction dynamics (Sun et al (2001, 2007)) has given a full description of the differential equations. The modelling is deployed as in-house FORTRAN code. This section presents the vehicle-track modelling, the wheel-rail interface modelling, and the model validation.

2.1 Vehicle-Track Modelling

Figure 1(a), 1(b), 1(c) and 1(d) show vehicle-track model called 3D-VTSD.

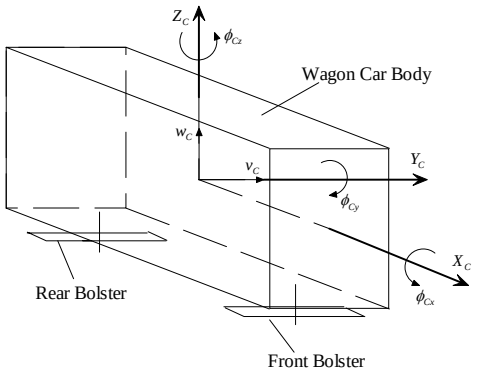

1(a) A Vehicle Car Body and Two Bolsters

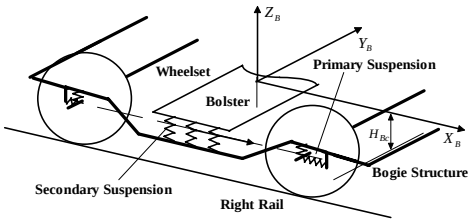

1(b) Bogie

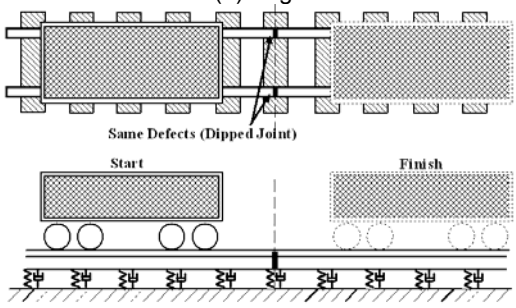

1(c) Track Longitudinal View

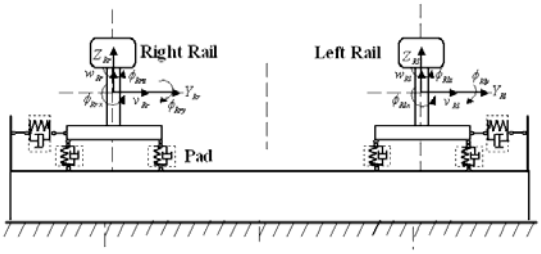

1(d) Track Lateral View

Figure 1 3D VTSD Model Representation

The Vehicle model includes one car body, two bolsters, two sideframes, and four wheelsets. All components are modelled as rigid bodies with six degrees of freedom (DoF) (lateral, vertical and longitudinal displacements, and roll, pitch and yaw rotations). The vehicle car body, as shown in Figure 1(a), rests on two bolsters through two centre bowls, and is longitudinally connected with two couplers, which are represented as springs. Nonlinear connection characteristics such as vertical lift-off and lateral and longitudinal impacts between sideframe and wheelset, sideframe and bolster, and bolster and vehicle car body are fully considered.

The track subsystem is considered as the discretely supported track with one layer as shown in Figure 1(c)

and 1(d). The track components are assembled exactly as the conventional ballasted track structure (e.g. sleeper spacing, pad and fastener stiffness, ballast modulus and depth, and subgrade modulus). The track model is structured as two Timoshenko beams, which represent two rails, supported by discretely distributed spring-damper elements, which represent the combined elasticity of rail pads and fasteners, ballast and subgrade. There are five DoFs at any point on the rail beam – lateral and vertical displacements (v_{Ri} and w_{Ri} ($i = l, r$)), and three rotations (ϕ_{Rix}, ϕ_{Riy} and ϕ_{Riz}) about longitudinal, lateral and vertical directions. Equivalent stiffness and damping coefficients have been used to take into account the stiffness and damping of rail pad, sleeper and ballast. In this track model, the effect of sleeper and ballast masses has been ignored.

For simplicity, the dynamic equilibrium equations of the rail beam have been expanded using a Fourier series in the longitudinal (X) direction by assigning an equal number of terms (n_m, also known as the number of modes of the rail beam) for both the linear displacements and the angular rotations.

2.2 Wheel-Rail Interface Modelling

For the wheel-rail interface, the normal force due to wheel-rail rolling contact is determined using Hertz static contact theory. The tangent creep forces and the creep moments are defined using Kalker's linear creep theory. The comprehensive model includes the vertical and lateral velocities of the rail in the definition of the creepages in the lateral and spin directions. The normal contact force F_{WTn} is determined using Hertz contact theory and can be expressed in Eq. (2):

$$F_{WTn} = \begin{cases} C_H [w_R - w_w - \mu(x)]^{3/2} & \text{if } w_R - w_w - \mu(x) > 0 \\ 0 & \text{if } w_R - w_w - \mu(x) < 0 \end{cases} \quad (2)$$

where C_H is Hertz contact coefficient, w_R and w_w are the vertical displacements of rail and wheel at the contact point, and $\mu(x)$ is the function representing the wheel or rail defects.

2.3 Solution Technique

For the vehicle model the equations of dynamic equilibrium may be written using multi-body mechanics methods. For the track model the lateral and the vertical bending and shear deformations of the rail are described using Timoshenko beam theory in addition to considering the torque of the rail beam. After applying a Fourier series expansion in the longitudinal direction, the equations of dynamic equilibrium were obtained for the rails. The equations of dynamic equilibrium for wagon and track modelling are expressed in Eq. (3):

$$\begin{bmatrix} M_W & 0 \\ 0 & M_T \end{bmatrix} \begin{Bmatrix} \ddot{d}_W \\ \ddot{d}_T \end{Bmatrix} + \begin{bmatrix} C_W & 0 \\ 0 & C_T \end{bmatrix} \begin{Bmatrix} \dot{d}_W \\ \dot{d}_T \end{Bmatrix} + \begin{bmatrix} K_W & 0 \\ 0 & K_T \end{bmatrix} \begin{Bmatrix} d_W \\ d_T \end{Bmatrix} = \begin{Bmatrix} F_{WT} \\ \tilde{F}_{WT} \end{Bmatrix} \quad (3)$$

Where M_W and M_T, C_W and C_T, and K_W and K_T are the mass, damping and stiffness matrices of wagon/track modelling. Parameter d_W is the displacement vector of the wagon subsystem, and vector d_T contains displacement of the track subsystem that includes the modal and physical displacements. Parameter F_{WT} is the wheel-rail interface force vector consisting of the wheel-rail normal contact forces, tangent creep forces and creep moments about the normal direction in the wheel-rail contact plane. Parameter $\tilde{F}_{WT}$ is the combined wheel-rail interface force vector. A modified Newmark $-\beta$ method is employed to solve Eq. (3).

2.4 Modelling Validation

In a selected track line, it was found that there were a number of rail top defects throughout the site, associated with the dipped welds, squats and top defects due to fouled ballast. Figure 2(a) and 2(b) illustrate two squats defects, and their measurements using a 1.0 metre dip gauge are presented in Figure 2(c) and 2(d).

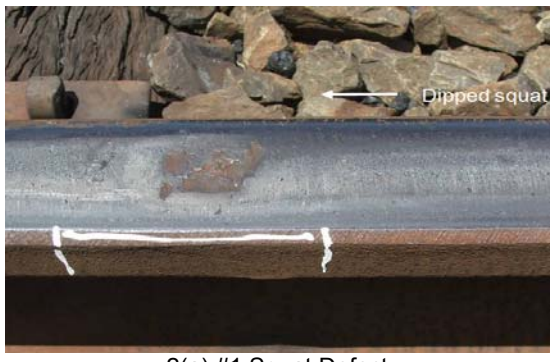

2(a) #1 Squat Defect

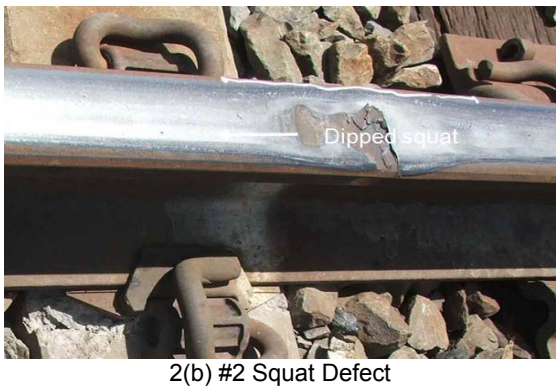

2(b) #2 Squat Defect

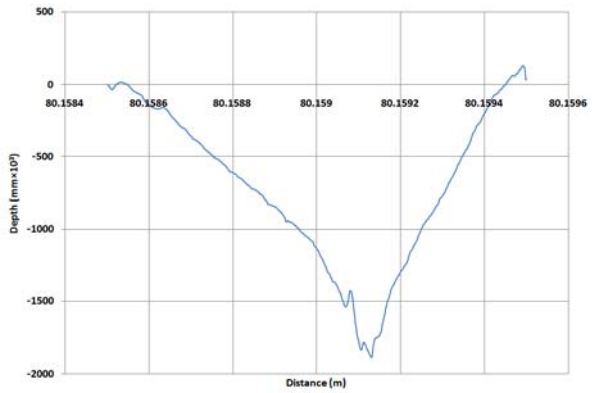

2(c) Profile Corresponding to #1 Defect

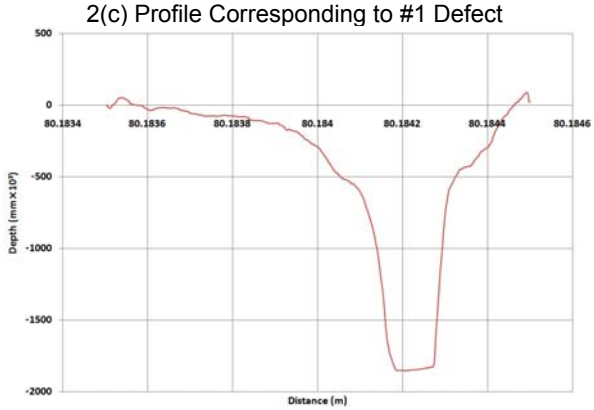

2(d) Profile Corresponding to #2 Defect

Figure 2 Single Dip Measured Profiles

When a rail vehicle (its parameter data is given in Appendix-I) passed through these two defect locations, significant wheel impacts were generated. The accelerometers were installed on the axle boxes (Figure 3(a)), from which the impact accelerations were recorded as shown in Figure 3(b).

3(a) Accelerometers

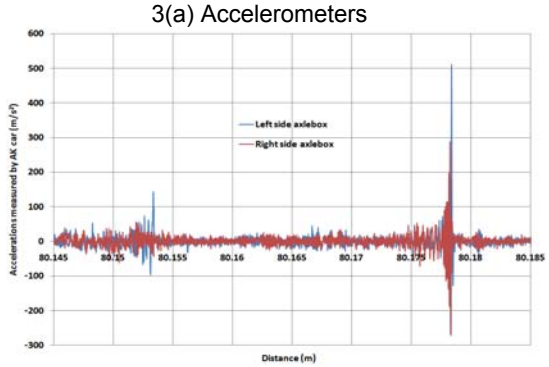

3(b) Acceleration data

Figure 3 Acceleration Measurements

Figure 4 compares the measured results with the results from the 3D VTSD model simulations.

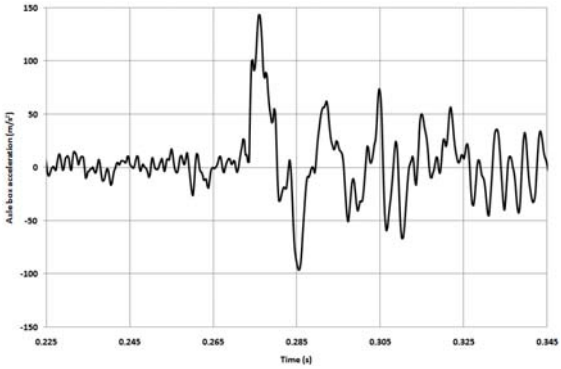

4(a) Measured Acceleration due to #1 Defect

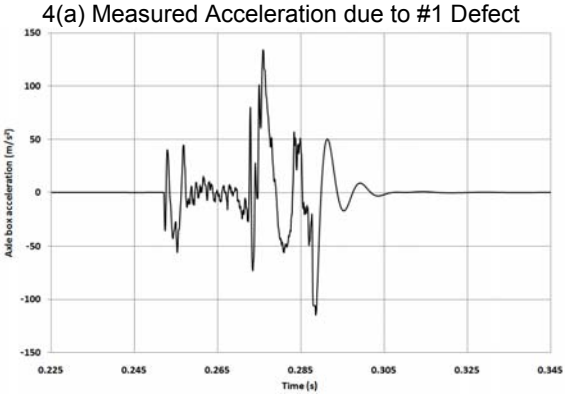

4(b) Simulated Acceleration due to #1 Defect

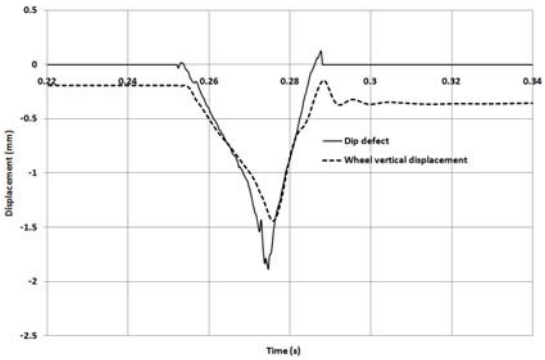

4(c) Dip defect and Wheel displacement due to #1 Defect

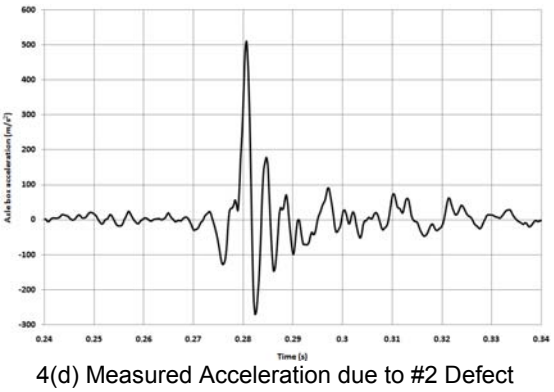

4(d) Measured Acceleration due to #2 Defect

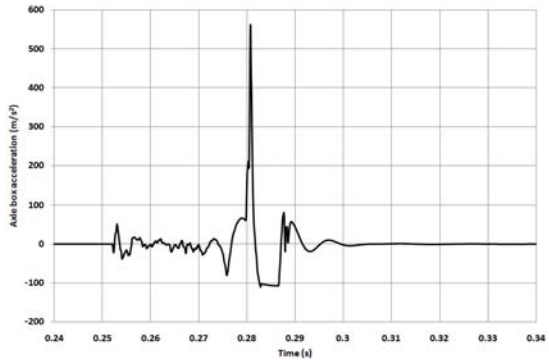

4(e) Simulated Acceleration due to #2 Defect

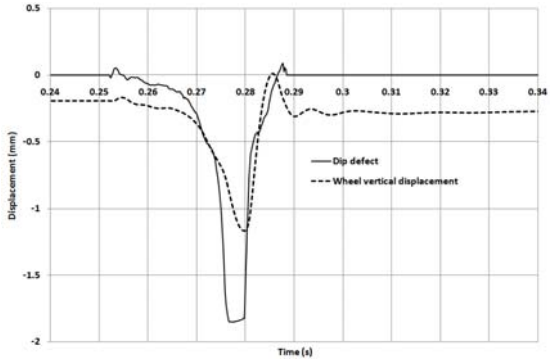

4(f) Dip defect and Wheel displacement due to #2 Defect

Figure 4 Measured and Simulated Results

From the comparison of measured and simulated accelerations, it can be seen that the simulated results are in good agreement with the measured ones. For the larger dip defects as shown in Figure 2(b) and 2(d), the simulations indicated that after the wheel enters the defect, the wheel will separate with the rail and briefly fly over the rail, leading to a zero contact force. When the wheel lands on the rail, a larger wheel impact will be generated (Figure 4(d) and 4(e)). From the simulated wheel displacements shown in Figure 4(c) and 4(f), it is evident that the wheel cannot touch the bottom of these particular defects, as the wheel displacements cannot follow the defect profiles.

3. Application of the P_2 Force Equation

An example for the application of P_2 force equation (Eq. (1)) is from the Rail Industry Safety and Standard Board (RISSB), Australia [11]. In its application, K_t is nominally taken as 109MN/m, C_t is 52kNs/m, and M_t is 133kg. From Eq. (1), it can be seen that P_2 changes linearly with the static wheel load, the dip angle and the speed, and nonlinearly with the unsprung mass, the track parameters – equivalent stiffness, damping and mass. It can be also seen that the dip angle only affects P_2 regardless of how large a dip defect is. According to [11], the P_2 force exerted by rollingstock travelling at its nominal maximum speed and nominal gross mass over a dipped weld in one rail shall not exceed the limits set out in Table 1.

Table 1

Route	Rail size (kg/m)	P2 force limit (kN)	
		0.010 rad dip	0.014 rad dip
Interstate standard gauge network	≥ 53	200	
Railcorp Class 1 track	≥ 53	(192)	230
Railcorp Class 2 track	< 53	(192)	230
1067mm gauge track	≥ 41	200	
Note: Figures in brackets are approximate figures scaled for 0.01 radian dip			

The unsprung mass is defined approximately as the mass between the rail and the bogie suspension. For the vehicle (its parameter data are given in Appendix-I), the effective unsprung mass is M_u = 1120 kg, and the static wheel load is P_0 = 57.575 kN.

3.1 P_2 Force via Speed V, Dip Angle α and Unsprung Mass

In this situation, the parameters are selected using the nominal values as shown below:

- K_t = 109MN/m
- C_t = 52kNs/m
- M_t = 133kg
- P_0 = 57.575 kN

Figure 5(a), 5(b) and 5(c) show the relationship between the calculated value of P_2 & speed, P_2 & dip angle, and P_2 & unsprung mass.

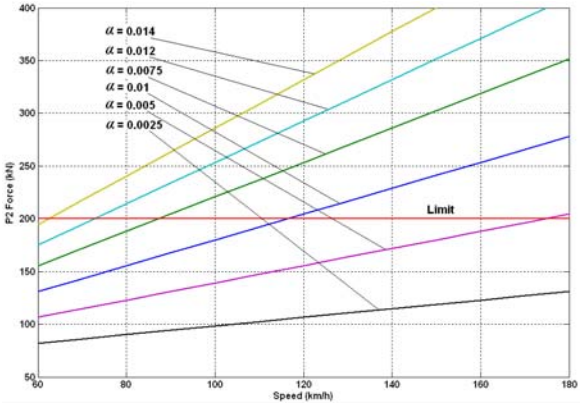

5(a) P_2 and Speed

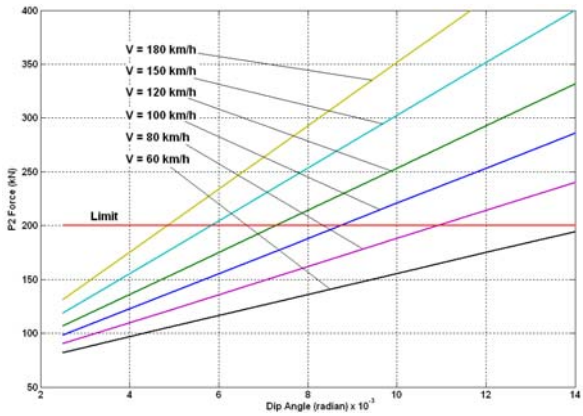

5(b) P_2 and Dip Angle

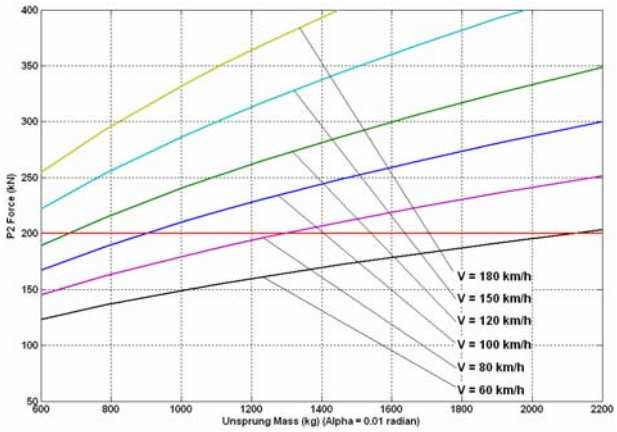

5(c) P_2 and Unsprung Mass (at α = 0.01 radian)

Figure 5 Relationship between P_2 and Speed, Dip Angle and Unsprung Mass

It can be seen from Figure 5 that the P_2 force increases as the speed, dip angle and the unsprung mass increase. For examples, in Figure 5(a) at α = 0.01 radian and when the speed changes from 60 km/h to 120 km/h (a 100% increase), the P_2 force increases from 155.5 kN to 253.65 kN (a 63% increase). In Figure 5(b), at V = 100 km/h and when the dip angle increases from 0.006 to 0.012 (a 100% increase), the P_2 force increases from 156 kN to 254.5 kN (a 63.7% increase). In Figure 5(c), at the conditions of α = 0.01 radian and V = 100 km/h, and when the unsprung mass increases from 800 kg to 1600 kg (a 100% increase), P_2 increases from 190.3 kN to 258.6 kN (a 35.9% increase). It can be seen that the speed and the dip angle have a similar influence on the P_2 force, and that this influence on P_2 is much larger than that for the unsprung mass.

3.2 P_2 and Track Parameters

In this situation, the parameters are selected as below:

- α = 0.01 radian
- P_0 = 57.575 kN
- M_u = 1120 kg

Figure 6(a), 6(b) and 6(c) show the relationship between P_2 and track parameters.

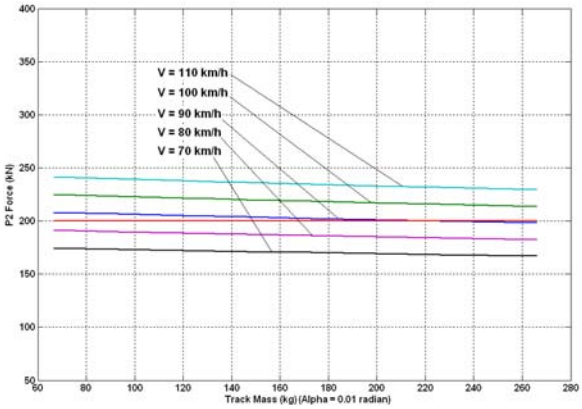

6(a) P_2 and Track Mass

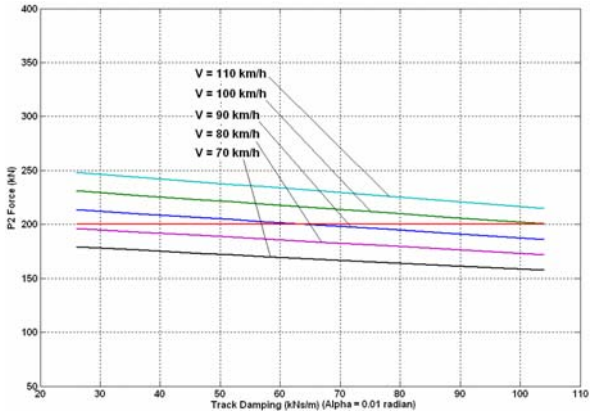

6(b) P_2 and Track Damping

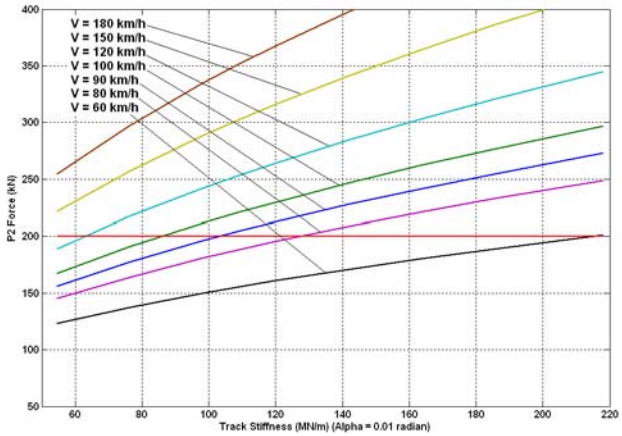

6(c) P_2 and Track Stiffness

Figure 6 Relationship between P_2 and Track Parameters

It can be seen from Figure 6 that P_2 decreases as the track mass and damping increase. However, P_2 increases as the track stiffness increase. For example, in Figure 6(a), at the speed of 90 km/h and when the track mass increases from 100 kg to 200 kg (a 100% increase), the P_2 force decreases from 206.3 kN to 201 kN (a 2.6% decrease). In Figure 6(b), at V = 90 km/h and when the track damping increases from 40 kNs/m to 80 kNs/m (a 100% increase), the P_2 force decreases from 208.4 kN to 194.6 kN (a 6.6% decrease). In Figure 6(c), at V = 90 km/h, when the track stiffness increases from 80 MN/m to 160 MN/m (a 100% increase), P2 increases from 180 kN to 238.6 kN (a 32.6% increase). It can be said that the track mass and track damping do not significantly influence P_2 compared with the track stiffness.

4. Simulations Using 3D VTSD Model

4.1 Rail Dip Modelling

The rail dip defect model is well-known and illustrated in Figure 7 and expressed as Eq. (4).

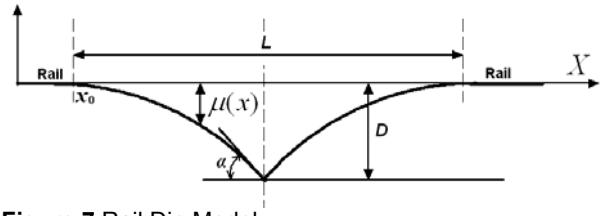

Figure 7 Rail Dip Model

where *L* is the dip length (m), *D* is the dip depth (mm) and *α* is the dip angle (radian).

The rail joint dip can be expressed as:

$$\mu(x) = \begin{cases} -D[1-\cos(2\pi\dfrac{x-x_0}{2L})] & x_0 \le x < x_0 + L/2 \\ -D[1+\cos(2\pi\dfrac{x-x_0}{2L})] & x_0 + L/2 \le x \le x_0 + L \\ 0 & x > x_0 + L \end{cases} \quad (4)$$

4.2 Relation of P_2 to Dip Angle

Generally, in the wheel dynamic force the low frequency P_2 force is superimposed over the high frequency P_1 force in Figure 8(a). The P_2 force was sometimes better represented after averaging or low-pass filtering. The P_2 force in Figure 8(a) is obtained using low-pass filtering with the cut-off frequency of 600 Hz shown in Figure 8(b).

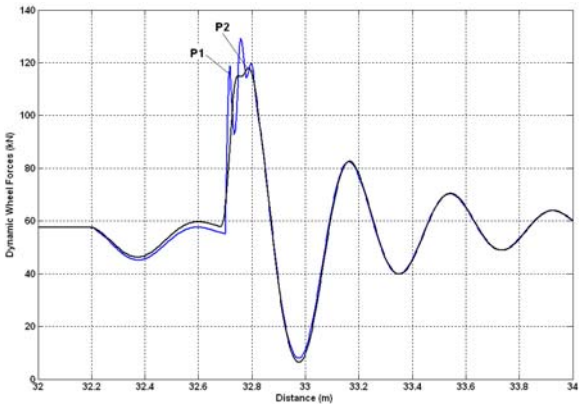

8(a) P_1 and P_2 forces

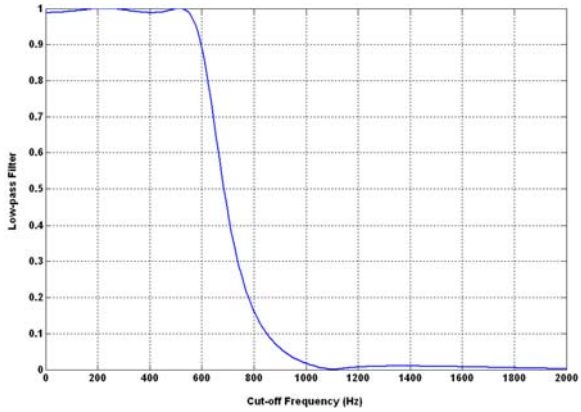

8(b) Low-pass Filtering

Figure 8 P_1 and P_2 Forces

The following simulations have been done to confirm whether or not the P_2 force is correlated to the dip angle *α* irrespective of what the dip length is, as stated in Eq. (1). In this scenario, the track stiffness and damping are selected to be the same as those in Section 3.1, namely, K_t = 109MN/m and C_t = 52kNs/m. The wheel dynamic force, vertical axlebox acceleration and displacement for the dip length range of 0.1 ~ 1.4 m, dip angle range of 0.005 ~ 0.014 radian at the speed of 80 km/h are simulated. Figure 9 shows the results at the dip angles of 0.005 and 0.014 radians respectively. It can be seen from Figure 9(a) and 9(b) that P_2 is related to both dip angle and length.

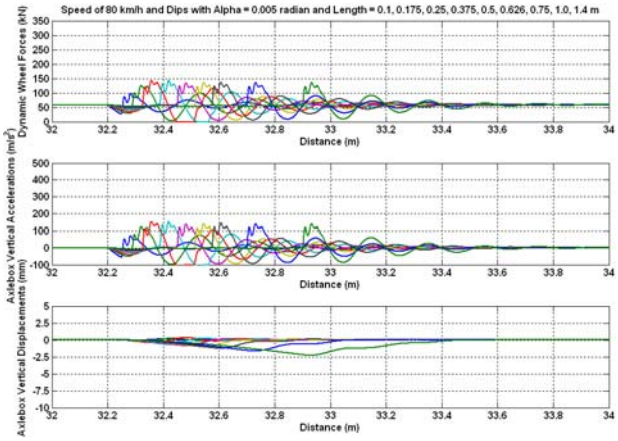

9(a) *α* = 0.005 radian

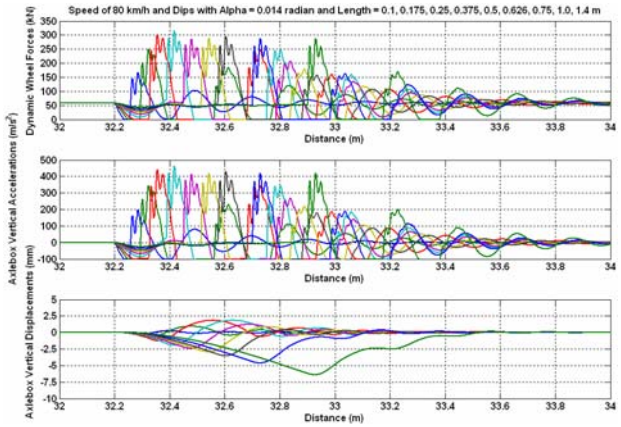

9(b) α = 0.0075 radian

Figure 9 Dynamic Responses at Speed of 80 km/h

Figure 10 shows the relationship between P_2 and the dip length under the influence of the dip angle being 0.005, 0.0075, 0.01 and 0.014 radians.

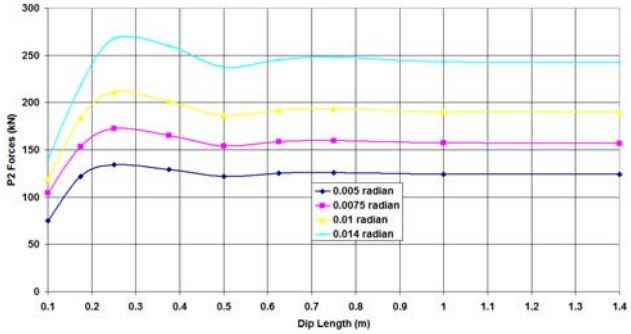

Figure 10 Relationship between P_2 and the Dip Length

From Figure 10, it seems that for the dip length larger than 0.5m the P_2 force remains constant for dip angle and independent of the dip length at the speed of 80 km/h. However, the dip length of 0.25m makes P_2 due to #2 Defect reach the maximum, and for the dip length less than 0.25, the P_2 is significantly reduced. Therefore, Eq. (1) is suitable to the larger dip length of rail joint dip, e.g., larger than 0.5 m for application in this paper.

The simulations have been extended to establish the relationship between P_2 and the dip angle for the dip length larger than 0.5 m. The track parameters remain unchanged. The wheel dynamic forces for the dip angle range of 0.0025 ~ 0.014 radian at the dip length of 1.0 m and the speed of 80 km/h are simulated. Figure 11(a) presents the wheel dynamic forces before and after filtering. Figure 11(b) presents the relationship between the maximum wheel dynamic force, the simulated P_2 force and the P_2 force from Eq. (1) and the dip angle.

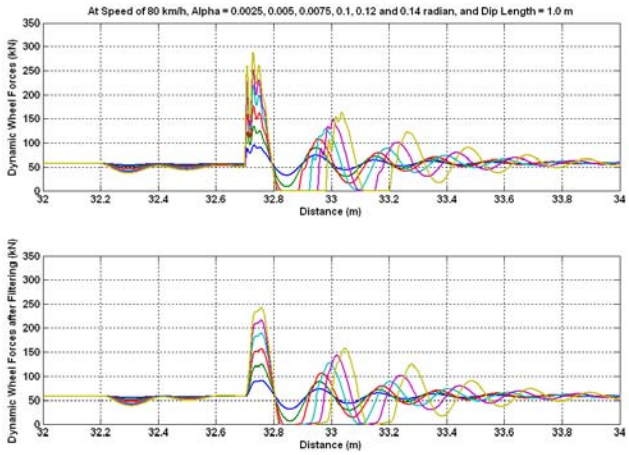

11(a) Before and after Filtering

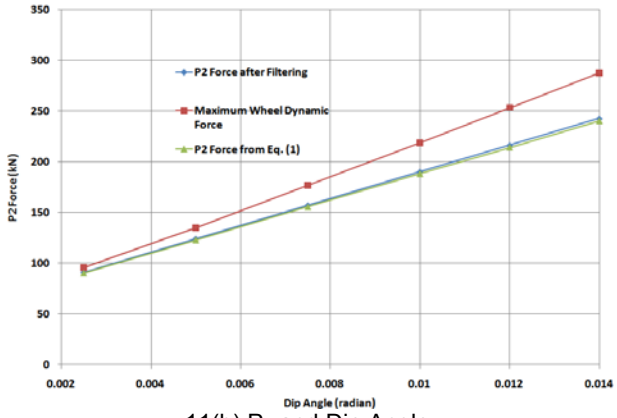

11(b) P_2 and Dip Angle

Figure 11 Relationship between P_2 and the Dip Angle

It can be seen from Figure 11(b) that the simulated value of P_2 is largely consistent with that from the Eq. (1), and both P_2 forces have a linear relationship with the dip angle.

4.3 Relation of P_2 to Speed

The following simulations have been undertaken to determine the relationship between P_2 and speed. The simulations are conducted for the dips with the dip length of 1.0m and the dip angles of 0.0025, 0.0075 and 0.014 radians respectively at the speed range of 20 ~ 150 km/h. The track parameters in the above section remain unchanged. Figure 12(a) presents the wheel dynamic forces before and after filtering at the dip angle of 0.0075 radian. Figure 12(b) compares the relationship between P_2 from the simulation and Eq. (1) and the speed.

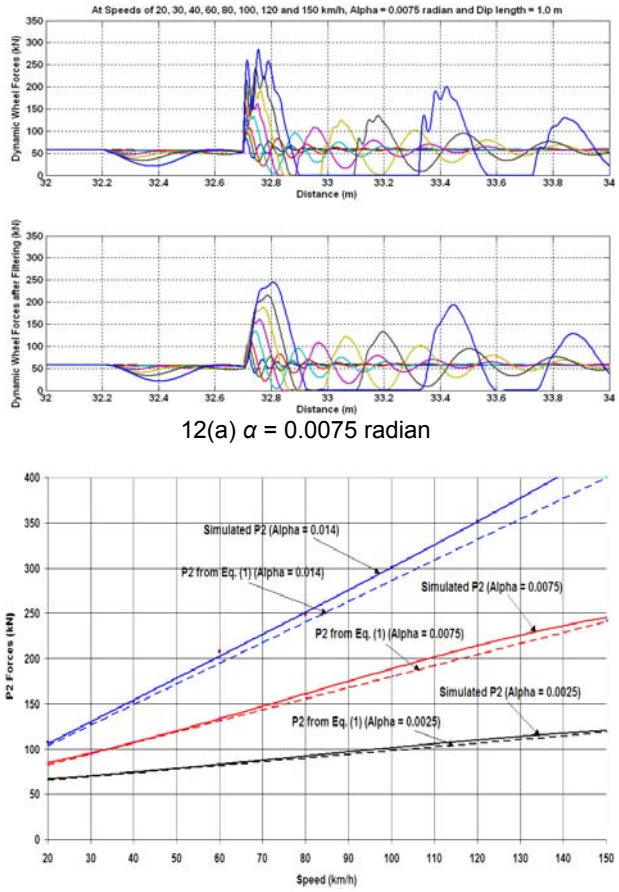

12(a) α = 0.0075 radian

12(b) P_2 Force and Speed

Figure 12 Relationship between P_2 and Speed

From Figure 12(b), it may be observed that P_2 and speed have a linear relationship. For a dip with smaller angle (e.g., 0.0025 radian), P_2 from the simulation and Eq. (1) have a very similar change as the speed increases. However, for a dip with a larger angle (e.g., 0.014 radian), the simulated P_2 force is generally higher than that from Eq. (1).

4.4 Other Dip Shapes

Although it is popular for a joint dip to be modelled in Eq. (2), other possible dip shapes are shown in Figure 13.

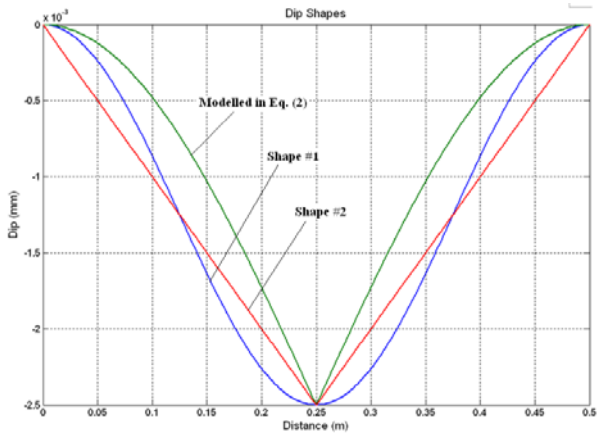

Figure 13 Dip Shapes

In Figure 13, the shape #1 is expressed as: $-\frac{1}{2}D\left(1-\cos\left(\frac{2\pi(x-x_0)}{L}\right)\right)$. The shape #2 is the straight line.

The simulations have been conducted for the three dip shapes shown in Figure 13 at the speed of 80 km/h. The wheel dynamic responses are provided in Figure 14.

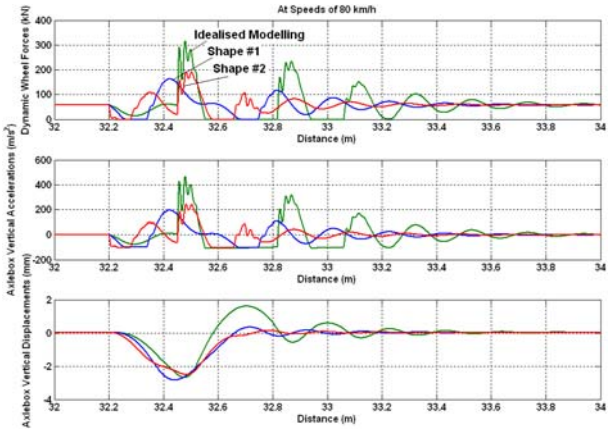

Figure 14 Wheel Dynamic Responses

In terms of dip angle, for the idealised dip modelling, α = D/Lπ = 2.5/500π = 0.0157 radian. For shape #1 the angle α = 0 and for shape #2, the angle α = 2D/L = 0.01 radian. Therefore, the wheel dynamic responses due to the idealised dip modelling are more severe than those due to the other two shapes. The wheel dynamic response due to the shape #1 is smooth which corresponds with the shape. For shape #1, P_2 force cannot be predicted using Eq. (1).

5. Closing Remarks

The wheel dynamic responses have been simulated using a detailed three-dimensional vehicle-track system dynamics model (3D VTSD model). The dip modelling has been idealised in an expression in Eq. (2). In such a dip model, some simulation results are in good agreement with the results based on the P_2 formula in Eq. (1).

However, in this paper for the dips with their length larger than 0.5m, the simulations have confirmed that P_2 is related to the dip angle regardless of the dip length as given in the P_2 equation. For the dips with larger dip angles (e.g., 0.014 radian), the simulated P_2 forces are reasonably agreeable with the values from the P_2 equation at a low speed. However, as the speed increases, the simulated P_2 forces are greater than those determined from the P_2 equation.

The 3D VTSD model may be used to predict the wheel dynamic force due to any rail dip defect shape, which is not possible using the P_2 equation (Eq. (1)).

ACKNOWLEDGEMENTS

Rail CRC Innovation Australia financially supported this research project. The support, involvement and encouragement of the colleagues of the Centre for Railway Engineering and the fellows of RailCorp, NSW are thankfully acknowledged.

REFERENCES

[1]. Jenkins, H.H., Stephenson, J.E., Clayton, G.A., Morland, G.W. and Lyon, D., 1974. The effect of track and vehicle parameters on wheel/rail vertical dynamic forces. Railway Eng. J. 3 1, pp. 2–16.

[2]. Cai, A, Raymond, G.P., 1992. Theoretical model for dynamic wheel/rail and track interaction, International Wheelset Congress Sydney Australia, 127-131.

[3]. Dahlberg, T., 1995. Vertical dynamic train/track interaction – verifying a theoretical model by full-scale experiments. Vehicle System Dynamics Supplement, 24, 45-57.

[4]. Shen, Z., 1991. On principles and methods to reduce the wheel/rail forces for rail freight vehicles. In: Proc. of 12th IAVSD Symposium, 584-595.

[5]. Dong, R.G., Sankar, S., Dukkipati, R.V., 1994. A finite element model of railway track and its application to the wheel flat problem. Proc Instn Mech Engrs, 208, 61-72.

[6]. Zarembski, A.M., 1995. Wheel/rail impact: P_1 and P_2 forces. Railway Track & Structures, 9-10.

[7]. Steenbergen, M. and Esveld, C., 2006, Relation between the geometry of rail welds and the dynamic wheel–rail response: numerical simulations for measured welds, Proc. IMechE Vol. 220 Part F: J. Rail and Rapid Transit, 409-423.

[8]. Zhai, W., Wang, K., Cai, C., 2009. Fundamentals of vehicle-track coupled dynamics, Vehicle System Dynamics, 1–28.

[9]. Sun, Y.Q., Dhanasekar, M., 2001. A dynamic model for the vertical interaction of the rail track and wagon system. International Journal of Solids and Structures, 39, 1337-1359.

[10]. Sun, Y.Q. and Simson, S., 2007. A Nonlinear Three-dimensional Wagon-track Model for The Investigation of Rail Corrugation Initiation on Curved Track. Vehicle System Dynamics, Vol. 45, No. 2, 113-132

[11]. www.rissb.com.au/UserFiles/file/Roll%2008-2%20Track%20Forces%20&%20Stresses%20-%20Freight%2028%20Jul%2006.xls

Appendix-I A Vehicle Model Parameters

1. Total mass	47Mg
2. Car body	
Mass	32.52Mg
I_x	75 Mg.m^2
I_y	227 Mg.m^2
I_z	200 Mg.m^2
Mass centre: x, y, z	0,0,1.75
Centre pivot: x, y, z	0,0,0.6
2 Bogie structure	
M	5Mg
I_x	3.0 Mg.m^2
I_y	3.5 Mg.m^2
I_z	5.0 Mg.m^2
Mass centre: x, y, z	8.0,0.0,0.60
3 Wheelset	
M	1.12Mg
I_x	0.73 Mg.m^2
I_y	0.03 Mg.m^2
I_z	0.73 Mg.m^2
Mass centre: x, y, z	9.23(6.77), 0.0, 0.46
Wheel radius: r_0	0.46
Wheel back gauge: b_w	Gauge =1.435; bw = 0.68
Wheel profile	QR Wheel LW3/QRAS60 Rail
4. Geometrical dimensions	
Semi-bogie centre: ab	8.0
Wheelset axle distance: a_w	2.46
5. Suspension	
5.1 The primary suspension:	
Top connection position: x, y, z	9.23(6.77), 1.2, 0.85
Bottom position: x, y, z	9.23(6.77), 1.2, 0.63
Spring radius: r_s	15mm
Parameters of a spring:	
n - effective circular	6
D1- radius of the outside spring	220mm
d1- diameter of the spring	30mm
D2 - radius of inside spring	150mm
d2 - diameter of the spring	15mm
H - high of spring	150mm
5.2 The secondary suspension:	
Top connection position: x, y, z	8.0, 1.3, 0.72
Bottom position: x, y, z	8.0, 1.3, 0.40
Spring numbers: ns	2
n - effective circular	Outside n1 = 7; inside n2 = 10
D1 - radius of the outside spring	230mm
d1- diameter of the spring	30mm
D2 - radius of the inside spring	150mm
d2- diameter of the spring	20mm
H- high of spring	320mm